*J. Electrochem. Sci. Eng.* **16** (2026) 3475; https://doi.org/10.5599/jese.3475

Open Access : : ISSN 1847-9286
https://pub.iapchem.org/ojs/index.php/JESE

*Original scientific paper*

# Bismuth-infused manganese molybdate nanostructures: a robust electrochemical platform for ultrasensitive uric acid detection

Chandraju Siddegowda Chidan Kumar[1,✉], Kuppahalli Sudarshan Mahesh Lohith[2], Mudaganduru Nagaraja Ramachandra[2], Mezna Saleh Altowyan[3], Payyanur Sumesh[1], Yarehalli Honnappa Pavithra[4] and Siddegowda Chandraju[5]

[1]*Department of Basic Science, Vidya Vikas Institute of Engineering & Technology, Visvesvaraya Technological University, Alanahalli, Mysuru 570028, Karnataka, India*
[2]*Department of Physics, ATME College of Engineering, 13th KM Stone, Mysuru-Bannur Road, Mysuru 570028, Karnataka, India*
[3]*Department of Chemistry, College of Science, Princess Nourah bint Abdulrahman University, P.O. Box 84428, Riyadh 11671, Saudi Arabia*
[4]*Department of Studies and Research in Chemistry, Tumkur University, Tumkur-572103, India*
[5]*Department of Chemistry, Sir MVPG Center, Tubinakere, Mandya University, Mandya 571402, Karnataka, India*

*Corresponding Author:* ✉*chidankumar.vviet@gmail.com*

Received: June 1, 2026; Accepted: August 18, 2026; Published: August 23, 2026

***Abstract***

*Sensitive and real-time monitoring of uric acid (UA) is essential for the effective management of metabolic disorders such as hyperuricemia and Lesch-Nyhan syndrome. Herein, $MnMoO_4$ (MMO) and bismuth-doped $MnMoO_4$ (BMMO) nanoparticles (NPs) were synthesized via a combustion method and employed to fabricate MMO-ME and BMMO-ME electrochemical sensors. $Bi^{3+}$ incorporation was associated with lattice distortion and improved electrochemical charge-transfer characteristics, as evidenced by the electrochemical measurements. Electrochemical studies revealed a diffusion-controlled, proton-coupled UA oxidation process with optimal response at physiological pH (7.0), while NP loading optimization identified 4 mg as the ideal composition. Compared to MMO-ME, the BMMO-ME electrode exhibited higher anodic current and lower peak-to-peak separation, and faster electron-transfer kinetics due to the synergistic bimetallic effect. Differential pulse voltammetry enabled ultrasensitive UA detection over a wide linear range (10 to 60 nM) with low detection limits of 5.0 (MMO-ME) and 4.5 nM (BMMO-ME). Both sensors demonstrated excellent stability, repeatability and reproducibility (RSD < 2 %), while BMMO-ME showed superior resistance to surface fouling. Accurate UA recovery (98 to 103 %) from tap water confirmed practical applicability. Overall, this work highlights Bi-induced defect engineering as an effective strategy to activate MMO*

*and establishes BMMO-ME as a robust, sensitive, and reliable platform for real-time UA biosensing.*

**Keywords**
$MnMoO_4$ nanoparticles; solution combustion; carbon paste electrode; differential pulse voltammetry; electrochemical sensing

## Introduction

Disorders of abnormal purine metabolism, including Lesch-Nyhan syndrome, reflect the fragility of uric acid (UA) homeostasis. Lesch-Nyhan syndrome is an X-linked hereditary disorder caused by deficiency of hypoxanthine-guanine phosphoribosyltransferase (HPRT), an essential enzyme in the purine salvage pathway [1,2]. When this pathway is impaired, purine base degradation increases, leading to excessive UA production. High UA concentrations lead to the deposition of monosodium urate crystals in the joints, kidneys, and soft tissues, causing an inflammatory response, nephrolithiasis, and problems with the kidneys [3]. Besides having metabolic abnormalities, patients have severe neurological and behavioural presentations, such as dystonia, developmental disorder, and compulsive self-harm behaviour [4]. The disorder is male-dominant and has a prevalence rate of about 1 per 380,000 live births [5]. Although pharmacological treatment can reduce UA levels, it does not enable continuous, real-time monitoring, which can prevent early diagnosis and accurate therapeutic management. This limitation highlights the need for analytical tools that can accurately and dynamically evaluate UA levels.

Uric acid is the product of purine degradation, which is the last one formed both by the intake of purines with food and endogenous nucleotide breakdown, where the liver is the main location of metabolism [6]. UA is a systemic antioxidant in circulation and plays a major role in plasma redox balance, primarily excreted by the kidneys [7]. The presence of high levels of uric acid (hyper-uricemia) causes monosodium urate crystallization, which causes gout, kidney stones, and progressive renal dysfunction [8]. On the contrary, low UA levels have been linked to rare metabolic disorders as well as subdued antioxidant defence [9]. Due to its limited physiological scope and clinical interest, precise and rapid analytical determination of UA in biological fluids is necessary yet technically challenging, which is why other analytical approaches have been developed.

Biosensors have also become promising analytical platforms for metabolite analysis because they integrate biological recognition components, including enzymes, antibodies, or nucleic acids, with transducers that convert biochemical responses into measurable outputs [10,11]. It can be integrated to enable rapid, selective, and sensitive detection, supporting timely clinical decision-making for conditions such as hyperuricemia [12,13]. In addition to clinical diagnostics, biosensors are widely used in environmental sensing, food safety, and pharmaceutical research, and enable the detection of pollutants, pathogens, and drug interactions [14,15]. The operation of biosensors, however, highly depends on the operation of the transducer material in terms of electrical conductivity, surface reactivity, stability, and biocompatibility [16,17]. Traditional electrode materials do not tend meet these demands, thereby limiting sensitivity and reproducibility and spurring the search for new functional materials.

Manganese molybdate ($MnMoO_4$) is an oxide of mixed transition metals, that has attracted considerable attention owing to its structural stability, chemical robustness, and rich redox chemistry [18-19]. The ease of electron transfer and electrocatalytic activity are enabled by the multiple oxidation states of manganese and molybdenum, making $MnMoO_4$ (MMO) a promising

candidate for electrochemical applications, including sensing and catalysis [20]. Although these benefits are apparent, pure MMO, in most cases, has moderate electrical conductivity and low surface affinity for biomolecules, which limits its direct use as a high-performance biosensor [21]. To overcome these limitations, dopant engineering has become a popular tool to provide electronic and surface modification of metal oxides.

Bismuth (Bi) is a post-transition metal with low toxicity, is extremely stable under electrochemical conditions, and has a high affinity for oxygen-containing species [22]. Incorporated into the lattices of oxides, Bi ions, along with their comparatively large ionic radius and the presence of an active lone pair of electrons, may lead to the formation of lattice distortion, oxygen vacancies, and electronic band structures [23]. These effects improve the mobility of charge carriers and interfacial electron transfer, which are essential in electrochemical sensing applications [24]. Bismuth-based composites have been shown to possess better catalytic activity, broader operating potential windows, and greater surface fouling resistance in electrochemical systems [25,26]. However, the effect of $Bi^{3+}$ doping on MMO, with reference to biosensing applications, remains underexplored.

Despite the growing interest in manganese-based molybdates for electrochemical applications, systematic studies addressing the role of aliovalent dopants in tailoring the defect chemistry and interfacial electron-transfer behaviour of MMO remain limited, particularly in the context of biosensing. In this regard, the present work reports the combustion-assisted synthesis of MMO and $Bi^{3+}$-doped MMO (BMMO) nanostructures and provides a comprehensive investigation of the dopant-induced modulation of their physicochemical and electrochemical properties. The incurporation of $Bi^{3+}$ ions into the MMO lattice is anticipated to induce lattice distortion, oxygen vacancy formation, and a rearrangement of the electronic structure, thereby enhancing charge-carrier mobility and increasing the density of catalytically active surface sites. A combination of X-ray diffraction and scanning electron microscopy was employed to establish phase purity, crystallinity, and morphology, while cyclic voltammetry (CV) and Differential pulse voltammetry (DPV) were utilized to elucidate redox kinetics, electrocatalytic efficiency and sensing performance toward UA oxidation. By correlating structural defects with electrochemical response, this study not only clarifies the fundamental role of Bi doping in MMO but also introduces a defect-engineering strategy for optimizing mixed-metal oxides, positioning BMMO as a promising and robust electrode material for sensitive, selective and reliable electrochemical biosensing applications.

## Experimental

### *Materials and reagents*

Ammonium heptamolybdate tetrahydrate [$(NH_4)_6Mo_7O_{24}{\cdot}4H_2O$, extra pure], manganese(II) nitrate hydrate [$Mn(NO_3)_2{\times}H_2O$, 99.9 %] and bismuth(III) nitrate pentahydrate [$Bi(NO_3)_3{\cdot}5H_2O$, 99.99 %] were purchased from Sigma-Aldrich India. Urea [$CON_2H_4$, 99.5 %], dopamine hydrochloride ($C_8H_{12}ClNO_2$, ≥98 %), uric acid ($C_5H_4N_4O_3$, ≥99 %), potassium ferrocyanide trihydrate ($K_4[Fe(CN)_6]{\cdot}3H_2O$, ≥98.5 %), potassium chloride (KCl, ≥99.5 %), sodium phosphate monobasic monohydrate ($NaH_2PO_4{\cdot}H_2O$, ≥98 %), and sodium phosphate dibasic heptahydrate ($Na_2HPO_4{\cdot}7H_2O$, ACS, 98 to 102 %) were purchased from Sisco Research Laboratories (SRL, India). The phosphate salts were used to prepare 0.2 M phosphate-buffered saline (PBS) at the required pH. All chemicals were of analytical grade and used as received without any further purification. Deionized water was used throughout the synthesis process.

*Synthesis of $MnMoO_4$ and $Bi^{3+}$-doped $MnMoO_4$ nanoparticles*

MMO and BMMO nanoparticles (NPs) were synthesized *via* solution combustion synthesis, using metal nitrates as oxidants and urea as a fuel. For the preparation of MMO, stoichiometric quantities of $Mn(NO_3)_2$ and $(NH_4)_6Mo_7O_{24}$ were dissolved in deionized water under continuous magnetic stirring to obtain a homogeneous precursor solution, followed by the addition of $CON_2H_4$ to achieve a near-stoichiometric redox balance. In the case of BMMO, bismuth (III) nitrate pentahydrate corresponding to 1 mol.% $Bi^{3+}$ was introduced into the precursor solution prior to fuel addition. The resulting precursor solutions were stirred for 30 min and transferred into a heat-crystalizing dish, which was then placed in a preheated muffle furnace maintained at 500 °C. Rapid dehydration followed by spontaneous ignition initiated a self-propagating combustion reaction, producing voluminous, porous powders due to the evolution of gaseous by-products. The as-combusted products were gently ground and subsequently calcined at 900 °C for 2 h in air to improve crystallinity and phase purity. The obtained MMO and BMMO NPs were used for further characterization and application studies (Figure 1a).

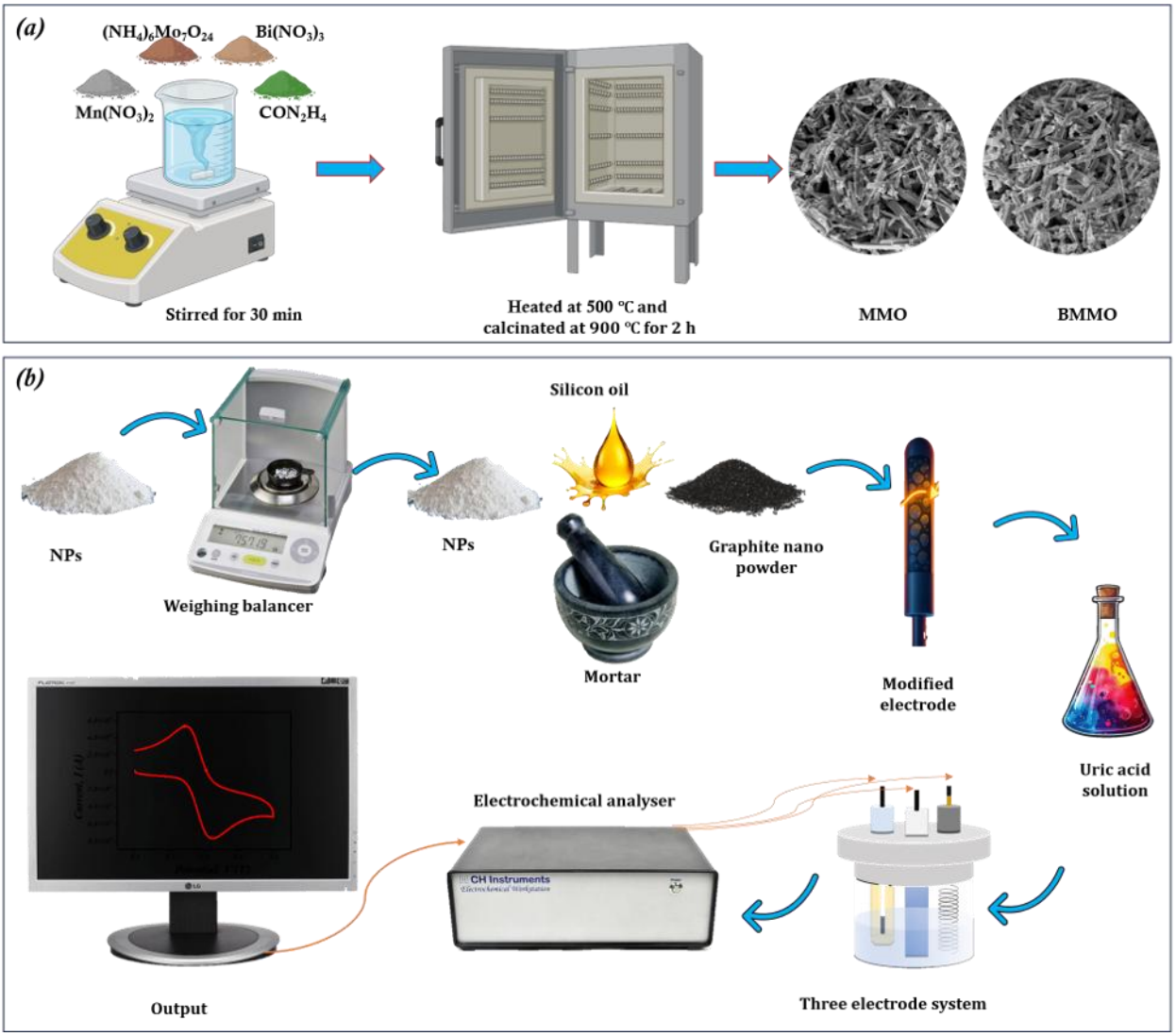


***Figure 1.*** *(a) Schematic illustration of the solution combustion synthesis route employed for the preparation of MMO and BMMO NPs. (b) Fabrication process of the BE, MMO-ME, and BMMO-ME*

*Preparation of bare carbon paste electrode and modified electrodes ($MnMoO_4$ and $Bi^{3+}$-doped $MnMoO_4$)*

The MMO-ME was prepared by mixing the optimized amount of MMO NPs with graphite powder and silicone oil at a 70:30 mass ratio to obtain a homogeneous, electrically conductive, and mechanically workable carbon paste. The mixture was well blended to obtain a homogenous distribution of NPs, which is essential in the development of a high density of electroactive sites. The resulting paste was then pressed into an electrode holder, taking care not to leave any air gaps to allow uniform electrical contact and mechanical stability (Figure 1b). The homogeneously dispersed MMO NPs also contributed to the electron-transfer pathway and significantly increased the electroactive surface area, enabling effective and rapid electrocatalytic oxidation of UA. CV results showed that MMO-ME exhibited higher anodic currents and lower overpotentials than the BE, indicating improved electrochemical activity due to the MMO modification.

To enhance the electrode's electrocatalytic properties, BMMO-ME NPs were synthesized and incorporated into the electrode to form BMMO-ME. Introduction of $Bi^{3+}$ ions into the MMO structure caused lattice distortions, the formation of oxygen vacancies, and a change in the electronic band structure, which in turn increased charge-carrier velocity and interfacial electron-transfer ratios. To produce a stable, homogeneous paste of the BMMO NPs, graphite and silicone oil were homogeneously added to the NPs, which were then carefully packed into the electrode holder. This bimetallic modification strongly increased the catalytic site count, conductivity, and electron-transfer rate, as well as anodic peak currents ($I_{pa}$), stability, and reduced overpotentials, compared with MMO-ME. Both electrodes exhibited high reproducibility and structural stability, but the electrocatalytic efficiency, long-term stability, and sensitivity of BMMO-ME were superior to those of MMO-ME; thus, it is a better platform for reliably and selectively detecting UA in complex biological samples. These features resulted in the same dispersibility of NPs and homogeneity of pastes, which are important for ensuring a consistent level of performance; therefore, a careful fabrication process is important when constructing high-performance electrochemical sensors.

*Characterization*

Powder X-ray diffraction (PXRD) patterns were recorded using a Rigaku SmartLab diffractometer (Rigaku Corporation, Tokyo, Japan) with Cu Kα radiation (λ = 0.15406 nm). Surface morphology and elemental composition were analysed using a ZEISS scanning electron microscope equipped with an EDS detector (Carl Zeiss AG, Oberkochen, Germany). Electrochemical measurements, including CV, DPV and electrochemical impedance spectroscopy (EIS), were carried out using a CHI608F electrochemical workstation (CH Instruments Inc., Austin, TX, USA) with a conventional three-electrode configuration. The BE, MMO-ME or BMMO-ME (geometric diameter: 3 mm, geometric area: 0.071 $cm^2$) served as the working electrode; an Ag/AgCl (3 M KCl) electrode was used as the reference electrode, and a platinum wire was employed as the counter electrode. EIS measurements were performed over a frequency range of 100 kHz to 0.01 Hz by applying an AC perturbation amplitude of 5 mV at a DC potential of 0.30 V.

## Result and discussion

*Structural and morphological analysis*

PXRD was employed to investigate the phase purity and crystallographic structure of MMO and BMMO NPs. As shown in Figure 2a, all diffraction peaks of MMO are well indexed to the monoclinic $MnMoO_4$ phase (PDF#01-082-2166) with C2/m symmetry, confirming the formation of a single-

phase material [27]. The PXRD pattern of BMMO exhibits no additional reflections or impurity phases, indicating that $Bi^{3+}$ incorporation does not alter the fundamental crystal structure of MMO. A slight peak broadening and marginal shift are observed in the BMMO sample, suggesting localized lattice distortion arising from dopant incorporation. The site-selective substitution of $Bi^{3+}$ ions in the MMO lattice can be rationalized using ionic-radius and coordination-number considerations. In MMO, $Mn^{2+}$ ions occupy octahedral sites (CN = 6) with an ionic radius of 0.083 nm, whereas $Bi^{3+}$ ions in six-fold coordination possess a larger ionic radius of 0.103 nm. Ionic radius mismatch ($\Delta r$ / %) was calculated using the relation [28], as given in Equation (1):

$$\Delta r = \frac{\left|R_{\mathrm{h}}\mathrm{CN}\text{-}R_{\mathrm{d}}\mathrm{CN}\right|}{R_{\mathrm{h}}\mathrm{CN}}100 \tag{1}$$

Here, $R_{\mathrm{d}}$ and $R_{\mathrm{h}}$ denote the ionic radii of the dopant and the host cation, respectively, and CN is the coordination number. The calculated $\Delta r$ value for $Bi^{3+}$ substituting $Mn^{2+}$ is ~24.1 %, which is below the commonly accepted substitution threshold of 30 %, confirming that $Bi^{3+}$ ions can be accommodated at $Mn^{2+}$ sites without inducing secondary phases. In contrast, $Mo^{6+}$ ions occupy tetrahedral sites (CN = 4) with a significantly smaller ionic radius of 0.041 nm. Given the large-size mismatch and the unfavourable coordination environment, substitution of $Bi^{3+}$ at the $Mo^{6+}$ site is crystallographically improbable. Rietveld refinement of the PXRD patterns for MMO and BMMO (Figure 2b) demonstrates excellent agreement between the observed and calculated profiles, with minimal difference curves, confirming the reliability of the monoclinic C2/m structural model. The refined lattice parameters exhibit only minor variations upon $Bi^{3+}$ doping, indicating that the overall lattice symmetry and long-range structural order of MMO are preserved. A schematic representation of the crystal structure of BMMO is shown in Figure 2c. The monoclinic MMO structure consists of corner-sharing $MoO_4$ tetrahedra interconnected with $Mn/BiO_6$ octahedra, forming a robust three-dimensional framework. The substitution of $Bi^{3+}$ ions at $Mn^{2+}$ sites maintains the connectivity of the polyhedral network, thereby preserving the overall structural stability of the lattice. The average crystallite size of the NPs was estimated using the Scherrer equation [29], as given in Equation (2):

$$D = \frac{k\lambda}{\beta\cos\theta} \tag{2}$$

where $D$ is the crystallite size, $k$ is the shape factor ($k$ = 0.9), $\lambda$ is the X-ray wavelength, $\beta$ is the full width at half maximum (FWHM) of the diffraction peak (in radians), and $\theta$ is the Bragg angle. Both MMO and BMMO NPs exhibited comparable crystallite sizes of approximately ~34 nm.

The surface morphology and microstructural features of MMO and BMMO NPs were examined by SEM, and the corresponding images are shown in Figure 2d and 2e, respectively. Both samples exhibit a densely packed rod-like morphology with relatively uniform size distribution and well-defined grain boundaries. The observed agglomeration can be attributed to the high-temperature combustion process and subsequent calcination, which promote particle coalescence. The elemental composition and successful incorporation of $Bi^{3+}$ ions in BMMO were confirmed by energy-dispersive X-ray spectroscopy (EDS), as shown in Figure 2f. The EDS spectrum shows Mn, Mo, O, and Bi, with no extraneous impurity signals. The elemental distribution supports the effective doping of $Bi^{3+}$ into the MMO lattice and validates the synthesis strategy employed.

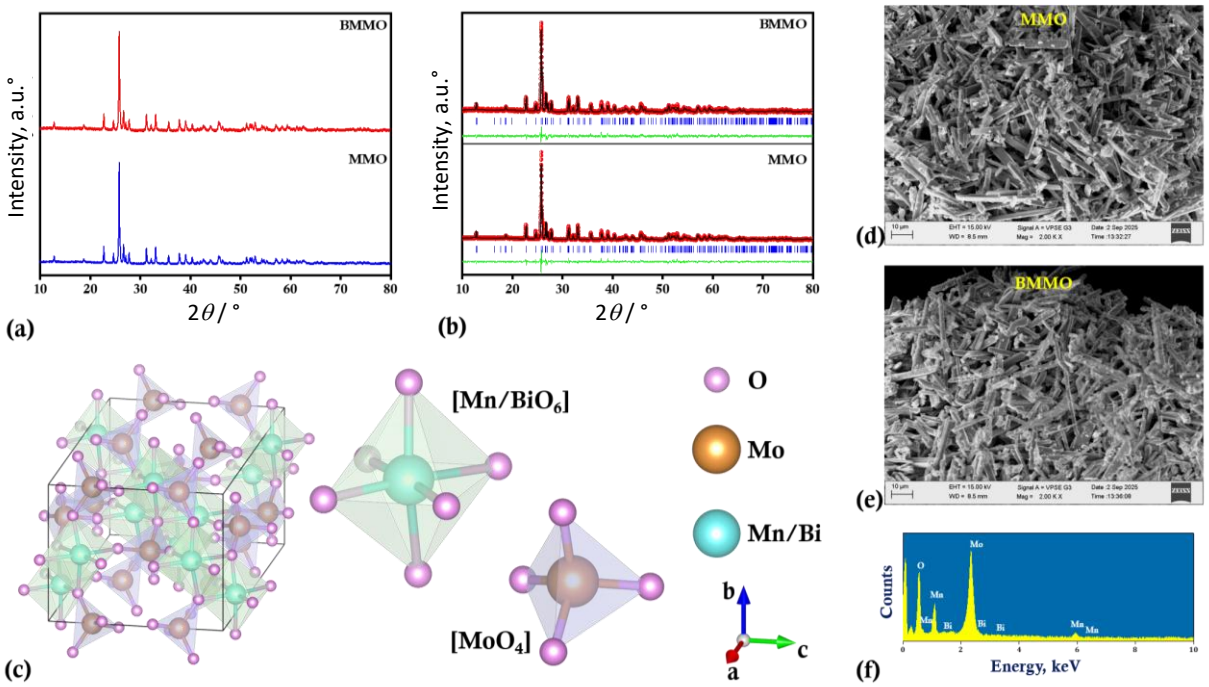


***Figure 2.*** *(a) XRD patterns and (b) Rietveld refinement profiles of MMO and BMMO NPs, (c) refined crystal structure of BMMO NPs, (d and e) SEM micrographs of MMO and BMMO NPs, (f) EDS spectrum of BMMO NPs*

*Optimization and electrochemical characterization of $MnMoO_4$ and $Bi^{3+}$-doped $MnMoO_4$ modified electrodes*

To optimize the active-material loading, MMO-ME and BMMO-ME electrodes containing 2, 4, 6, 8 and 10 mg of active material were evaluated by CV in 1 M KCl containing 25 mM $K_4[Fe(CN)_6]$ at a scan rate of 0.1 V $s^{-1}$ (Figure 3a and 3b). The anodic and cathodic peak currents increased with active-material loading up to 4 mg, then decreased at higher loadings. The decrease at higher loading may be associated with nanoparticle agglomeration and partial blockage of conductive pathways, reducing the number of electrochemically accessible sites [30]. Therefore, 4 mg was selected as the optimum active-material loading for both electrodes. Figure 3c compares the CV responses of the BE, MMO-ME, and BMMO-ME electrodes prepared using the optimized 4 mg loading.

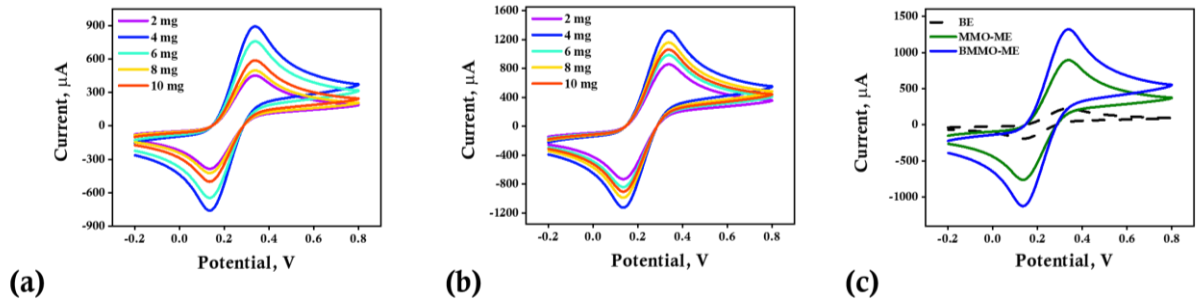


***Figure 3.*** *Effect of active material loading (2 to 10 mg) on the current response of the (a) MMO-ME and (b) BMMO-ME, (c) comparative CVs of the BE, MMO-ME, and BMMO-ME recorded using the 4 mg active material loading in 1 M KCl containing 25 mM $K_4[Fe(CN)_6]$ at a scan rate of 0.1 V $s^{-1}$*

The $I_{pa}$ increased from 231.6 µA for BE to 918.33 µA for MMO-ME and 1348 µA for BMMO-ME, while the cathodic peak current ($I_{pc}$) increased in magnitude from -197 to -770 µA and -1167 µA, respectively. The corresponding $\Delta E_p$ values decreased from 471 mV for BE to 458 mV for MMO-ME and 447 mV for BMMO-ME, indicating improved charge-transfer behaviour following electrode modification. The electroactive surface areas determined using the Randles-Ševčik equation were

0.09, 0.23 and 0.53 cm² for BE, MMO-ME and BMMO-ME, respectively. Although the relatively large $\Delta E_p$ values indicate a quasi-reversible redox process, BMMO-ME exhibited the highest redox current, the lowest $\Delta E_p$, and the largest electroactive surface area, demonstrating its improved electrochemical response [31-33]. The enhanced response of BMMO-ME is consistent with its increased electroactive surface area and the contribution of Bi incorporation to the electrode's charge-transfer characteristics.

*Electrochemical response of UA at $MnMoO_4$ and $Bi^{3+}$-doped $MnMoO_4$ modified electrodes depending on pH*

The electrochemical oxidation of UA at MMO-ME and BMMO-ME is highly sensitive to the electrolyte pH, providing evidence that the reaction is proton-coupled. The CV was conducted in 0.2 M phosphate-buffered saline (PBS) at pH 6.2 to 7.8 and a scan rate of 0.1 V $s^{-1}$ using 1 mM UA. The CV responses of MMO-ME and BMMO-ME are depicted in Figure 4a and 4b, respectively, at various pH.

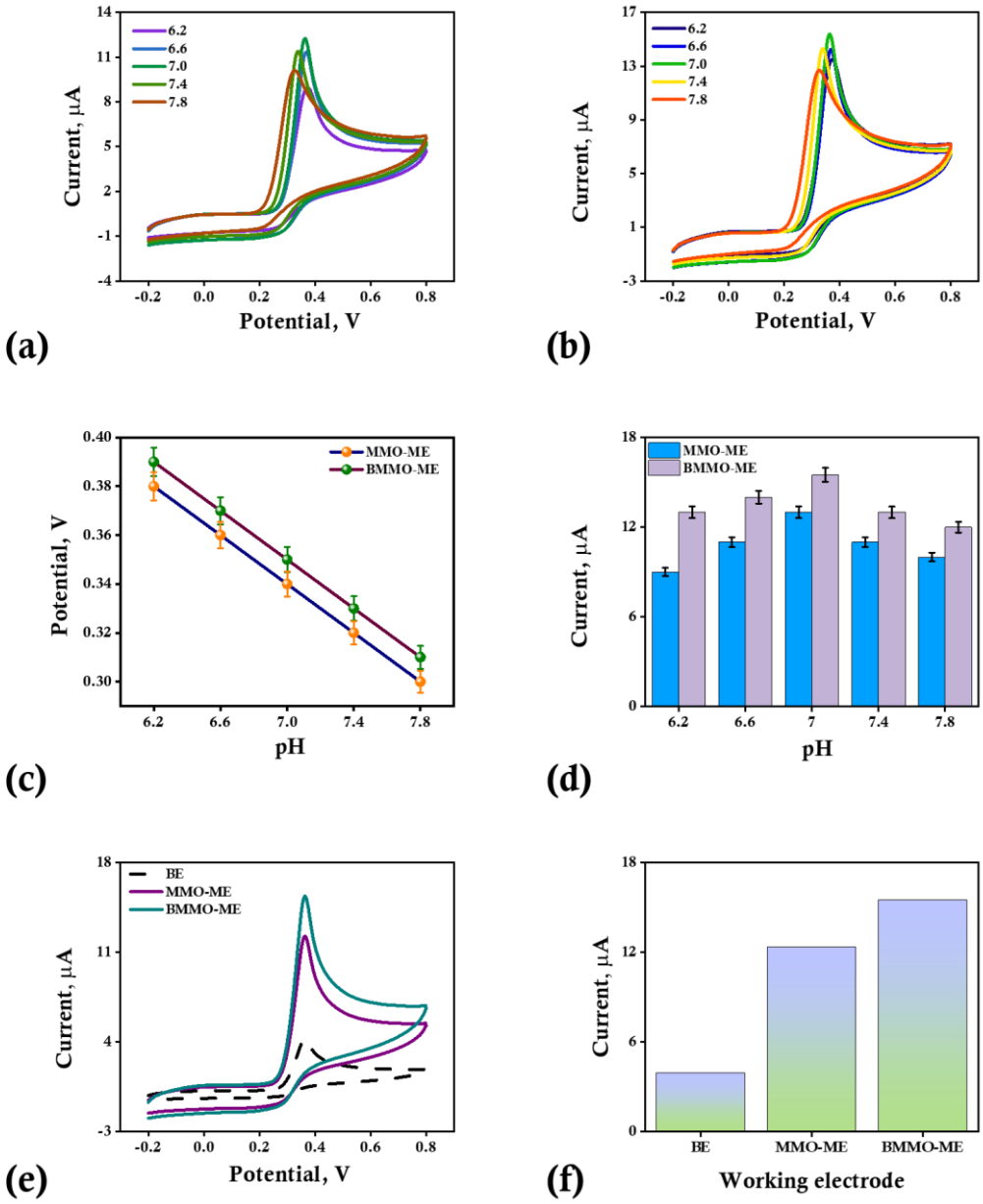


***Figure 4.*** *CV responses of (a) MMO-ME and (b) BMMO-ME toward 1 mM UA in 0.2 M PBS at different pH values (6.2 to 7.8), recorded at a scan rate of 100 mV $s^{-1}$, (c) variation of anodic peak potential with pH, (d) variation of anodic peak current with pH, (e) pH-dependent anodic peak current response identifying pH 7.0 as the optimum, (f) comparative CV responses of MMO-ME and BMMO-ME at pH 7.0 and 100 mV $s^{-1}$*

The $I_{pa}$ of the two electrodes increased with increasing pH towards 7.0, where physiological pH is located. This observation demonstrates that electron transfer between UA and the modified electrode surface is most favourable under near-neutral conditions, in which optimal proton availability and UA ionization at the electroactive sites promote effective adsorption and oxidation of UA [34]. After pH 7.0, the peak current decreased slightly, indicating that lower proton concentration reduces oxidation efficiency and underscoring the pivotal role of pH in controlling the electrochemical response. The anodic peak potential ($E_{pa}$) shifted to more negative values as pH increased, indicating a linear relationship for both MMO-ME and BMMO-ME. Figure 4c shows the Epa comparison graph, with slopes of about 0.050 and 0.051 V $pH^{-1}$ for MMO-ME and BMMO-ME, respectively, closer to the theoretical Nernstian slope of 0.059 V $pH^{-1}$ and suggesting an approximately equal proton-to-electron stoichiometric contribution to the electrode reaction [35]. Figure 4d compares the $I_{pa}$ of MMO-ME and BMMO-ME across the pH range, showing that BMMO-ME exhibits a greater electrochemical response, likely due to enhanced process kinetics or a stronger catalytic effect of Bi doping. Figure 4e indicates that the anodic peak is maximal at the highest response, measured at pH 7.0, underscoring the need to maintain physiological pH to achieve the best sensor response. Lastly, Figure 4f is a bar graph comparing the peak currents of MMO-ME and BMMO-ME at pH 7.0, and the electrochemical activity of the BMMO-ME electrode is superior to that of the pure MMO-ME electrode. These electrochemical responses indicate that MMO-ME and BMMO-ME can provide an effective platform for detecting UA under physically relevant conditions. The homogenous dispersion of NPs increases the electroactive surface area, leads to faster electron transfer, and is more sensitive [36]. However, pH must be strictly controlled to ensure reproducible values and maximize analytical performance, especially for BMMO-ME, which exhibits a higher current response owing to the catalytic contribution of Bi dopant atoms.

*Electrochemical kinetics*

Figure 5a represents the CV profiles of 1 mM UA at the MMO-ME at increasing scan rates from 50 to 500 mV $s^{-1}$. As the scan rate increases, $I_{pa}$ also increases proportionately, suggesting that a higher flux of electroactive UA molecules is delivered to the electrode surface within a shorter time window. This reaction shows that the MMO-ME nanostructure has sufficient electroactive surface area and catalytic sites that are accessible to facilitate rapid charge transfer. In addition to this improvement, the anodic peak potential gradually shifts positively at high scan rates. This change can be explained by higher ohmic drop and polarization due to faster potential sweeping, which prevents sufficient time to fully compensate the charges at the electrode-electrolyte interface [37]. The summation of the current and potential shift indicates that although UA oxidation is kinetically favourable at MMO-ME, diffusion-controlled bulk solution mass transport affects it. Figure 5b shows the scan-rate-dependent CV curves recorded at the BMMO-ME. BMMO-ME has a much larger $I_{pa}$ at all scan rates, thus indicating its better electrocatalytic response to UA oxidation than MMO-ME. This is due to the synergistic effect of the two metal components, which enhances electronic conductivity, the density of active sites, and the rate of electron transfer. The positive shift of the anodic peak potential with increasing scan rate is also smaller than that of MMO-ME, indicating reduced charge-transfer resistance and enhanced interfacial kinetics. The enhanced current response and reduced polarization effects confirm that BMMO-ME can readily promote UA oxidation even under high-potential scanning conditions, making it more suitable for high-sensitivity electrochemical sensing systems.

In Figure 5c, the electrochemical responses of MMO-ME and BMMO-ME were directly compared at a constant scan rate of 100 mV $s^{-1}$. BMMO-ME has a considerably higher $I_{pa}$ and a sharper, well-defined oxidation peak than MMO-ME at this optimized scan rate. The enhanced peak definition indicates rapid electron-transfer kinetics and reduced heterogeneity on the bimetallic electrode surface. The improved performance of BMMO-ME could be attributed to the cooperative catalytic effect of the bimetallic system, which enhances effective adsorption of UA molecules and speeds up their electro-oxidation. This comparison is supported by the fact that BMMO-ME is more effective and reliable as a sensing platform for detecting UA under physiologically relevant conditions.

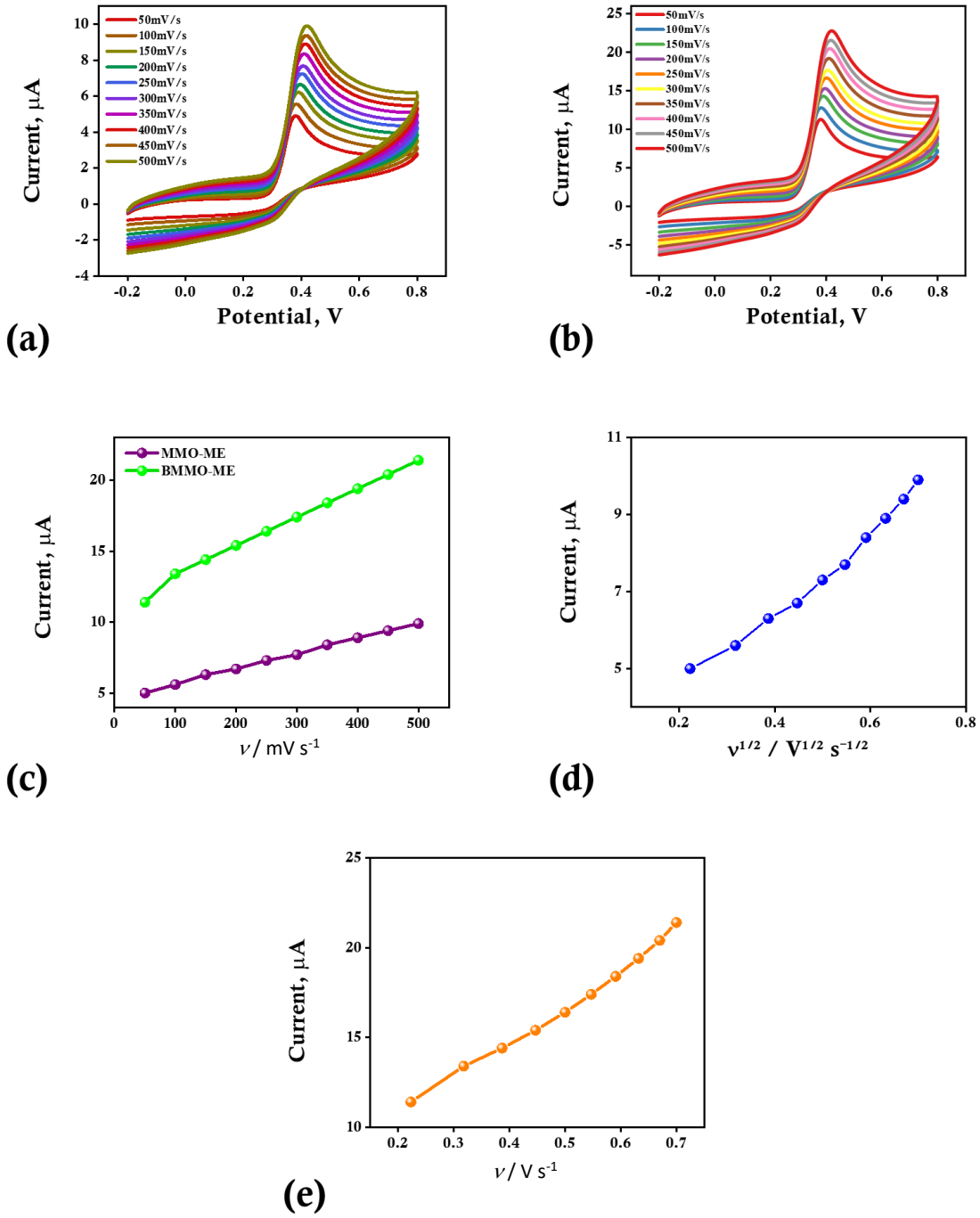


***Figure 5.*** *CV of (a) MMO-ME and (b) BMMO-ME recorded in 1.0 mM UA prepared in 0.2 M PBS (pH 7.0) at different scan rates, (c) variation of the anodic peak current with scan rate for the MMO-ME and BMMO-ME. Linear relationship between the anodic peak current and the square root of the scan rate for (d) MMO-ME and (e) BMMO-ME, indicating a diffusion-controlled electrochemical process*

Figure 5d shows the correlation of the $I_{pa}$ and the square root of the scan rate of MMO-ME. The plot shows very good linearity, suggesting that UA oxidation at MMO-ME occurs via a diffusion-controlled mechanism, with a coefficient of determination ($R^2$) of 0.99, indicating a strong linear correlation. This linear relationship suggests that UA oxidation at MMO-ME is predominantly diffusion-controlled and is consistent with the Randles-Ševčik equation [38]. This indicates that the movement of UA molecules between the bulk solution and the electrode surface is the rate-limiting step. The linear relationship between the $I_{pa}$ and the square root of the scan rate ($v^{1/2}$) indicates that the electrochemical oxidation of UA at the BMMO-ME is predominantly diffusion-controlled. Figure 5e shows the dependence of $I_{pa}$ on $v^{1/2}$ for the BMMO-ME, together with a comparative plot of scan rate versus peak current for both the MMO-ME and BMMO-ME, exhibiting excellent linearity ($R^2$ = 0.99). The linear behaviour suggests rapid mass transport of UA molecules to the electrode surface with negligible adsorption effects, confirming stable electrochemical performance and efficient electron-transfer kinetics during repeated scanning. The high linearity of BMMO-ME corroborates that UA oxidation at this electrode is also largely diffusion-controlled. Interestingly, the slope of the linear region of BMMO-ME is greater than that of MMO-ME, suggesting a more diffusion-limited current response and faster electron-transfer kinetics. This gain is associated with the increased catalytic performance and mass-transport properties provided by the bimetallic structure. The comparative study highlights the significance of bimetallic modification in optimizing diffusion-assisted electrocatalysis, ultimately resulting in excellent sensing performance.

*Electrode sensitivity*

Differential pulse voltammetry was used to examine the concentration-dependent electrochemical behaviour of MMO-ME and BMMO-ME towards UA detection because it is highly sensitive, provides high peak resolution, and can distinguish two closely spaced oxidation events [39]. The DPV results shown in Figure 6 indicate that as UA concentration increases, the $I_{pa}$ of both electrodes increases in the same proportion, whereas the anodic peak potential shows no significant variation, indicating efficient electron transfer and limited overpotential current at the modified electrode surfaces [40]. MMO-ME shows a definite and predictable current response, reflecting the increased electroactive surface area and catalytic activity provided by the metal oxide modification. However, BMMO-ME shows even higher peak currents under the same conditions, indicating that the bimetallic modification introduces new active sites, promotes faster electron transport, and further accelerates UA oxidation. The linearity of the concentration-peak current relationships, which is verified by calibration curves with regression coefficients close to 0.999, shows high reproducibility and reliability of both electrodes in quantitative analysis of UA. These findings underscore the importance of the electrode change in enhancing sensitivity, enabling fast electrocatalytic reactions, and providing a solid platform that can detect UA at physiologically relevant concentrations.

Figure 6a shows the DPV responses of MMO-ME toward different concentrations of UA (10 to 60 nM). With increasing concentration of UA, the current flowing through the anode increases in the same direction, and it is evident that there is a concentration-dependent electrochemical response. The anodic peak potential is almost independent of concentration, indicating an efficient electron transfer rate at the MMO-ME interface. This stability in peak potential also indicates low overpotential changes, suggesting that the electrode surface has a high concentration of active sites where UA oxidation occurs. The linear response means MMO-ME can provide predictable and reproducible UA concentrations; thus, it is applicable to the analysis of biological samples [41]. Also, the continuous rise in current shows that electrode modification increases the electroactive surface

area and the kinetics of charge transfer, which are better than those of unmodified electrodes. Figure 6b indicates that the DPV response of BMMO-ME under varied concentrations of UA was the same. BMMO-ME has a higher $I_{pa}$ at the same UA concentration, suggesting greater electron-transfer efficiency and increased effective electroactive surface area.

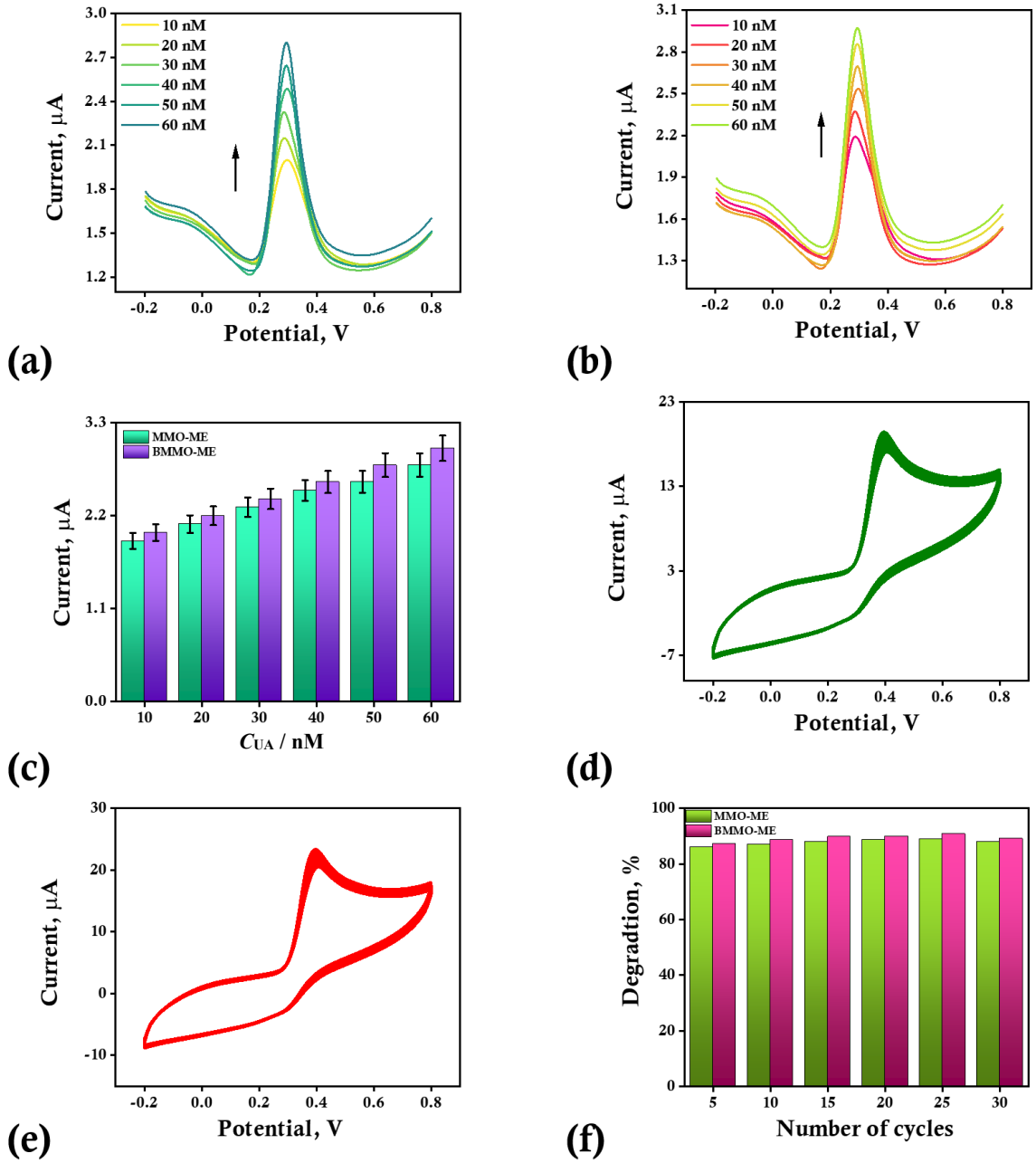


***Figure 6.*** *DPV responses of (a) MMO-ME and (b) BMMO-ME toward increasing concentrations of UA (10 to 60 nM) in 0.2 M PBS (pH 7.0), (c) comparison of anodic peak currents of MMO-ME and BMMO-ME at different UA concentrations. Stability performance of (d) MMO-ME and (e) BMMO-ME evaluated over 5 to 30 consecutive CV cycles in 1 mM UA in 0.2 M PBS (pH 7.0) at a scan rate of 100 mV $s^{-1}$, (f) comparison of current retention of MMO-ME and BMMO-ME during the stability test*

The anodic peak potential remains constant, showing that the electrode surface is stabilized by the bimetallic modification and that energy barriers to UA oxidation are reduced. This enhancement may be explained by the multi-effect of the two metal oxides in BMMO-ME, which provide more catalytic sites, enable faster electron transfer, and reduce charge-transfer resistance [42]. The findings indicate that BMMO-ME is more sensitive than MMO-ME and thus may be used to detect low-concentration UA with high specificity. Figure 6c shows a comparative bar graph of peak

currents for MMO-ME and BMMO-ME at varying UA concentrations. As shown in the Figure 6, BMMO-ME consistently generates higher currents than MMO-ME, reflecting the better electrocatalytic activity of the bimetallic electrode. This difference highlights the importance of electrode modification in enhancing electron transfer, increasing the number of active sites, and accelerating UA oxidation. The bar graph further emphasizes that the response improvement at higher UA concentrations is greater, indicating that BMMO-ME is particularly effective when higher analytical sensitivity is required.

Figure 6d shows the CV stability of MMO-ME over 5 to 30 consecutive cycles in 1 mM UA in 0.2 M PBS (pH 7.0) at a scan rate of 100 mV $s^{-1}$. The $I_{pa}$ shows a slight decrease with increasing cycle number, while the overall response remains relatively stable, indicating good repeatability. The decrease in current may be associated with gradual surface fouling or partial blocking of electroactive sites during repeated UA oxidation. Figure 6e shows the corresponding CV stability of BMMO-ME under the same conditions. BMMO-ME retains a higher proportion of its initial current response over successive cycles, indicating improved operational stability compared with MMO-ME. The higher current retention suggests that BMMO-ME provides a relatively stable electrode interface during repeated UA oxidation. Overall, these results demonstrate that both modified electrodes exhibit good short-term operational stability, with BMMO-ME showing better current retention than MMO-ME. Figure 6f provides a summarized graphic display of the stability performance of MMO-ME and BMMO-ME at 5 to 30 cycles. The plot shows that the electrochemical activity of both electrodes remains largely intact during the protracted measurements, with BMMO-ME retaining current better than MMO-ME. This comparison shows that the bimetallic change not only improves sensitivity but also makes the sensor much more stable under repeated use. The figure shows that both MMO-ME and BMMO-ME can serve as powerful platforms for detecting UA, with BMMO-ME offering additional benefits in catalytic efficiency, permanence, and feasibility for practical application in biosensing devices. The calibration plots obtained for MMO-ME and BMMO-ME electrodes exhibited excellent linearity over the concentration range of 10 to 60 nM, with a correlation coefficient of 0.99. Based on the $3\sigma/m$ and $10\sigma/m$ criteria, the limits of detection (LOD) and quantification (LOQ) were estimated to be 5.0 and 16.7 nM for the MMO-ME electrode, respectively, where $\sigma$ represents the standard deviation of the blank measurements and $m$ denotes the slope of the calibration curve. Notably, the BMMO-ME electrode demonstrated improved analytical performance, with lower LOD and LOQ values of 4.5 and 15.0 nM, respectively, highlighting the beneficial role of Bi doping in enhancing sensitivity by improving charge-transfer kinetics and increasing the availability of electroactive sites.

*Sensor robustness*

Figure 7a shows the CV responses of MMO-ME toward 1.0 mM UA in 0.2 M PBS (pH 7.0) over five successive measurements using the same electrode, demonstrating the repeatability of the electrode response. The current amplitude at the anode peak is virtually constant throughout the repeated scans, whereas there is an insignificant change in the potential of the anode peak. This indicates that electron transfer at the MMO-ME interface is extremely stable, and active sites for UA oxidation are not covered during repeated measurements [43]. The small current variation observed could be attributed to temporary adsorption of reaction intermediates or to moderate changes in experimental conditions, but these do not affect the electrode's overall sensitivity. These results justify the conclusion that MMO-ME is a reliable method to detect UA on repeated measures, which is why it can be used for real analytical purposes.

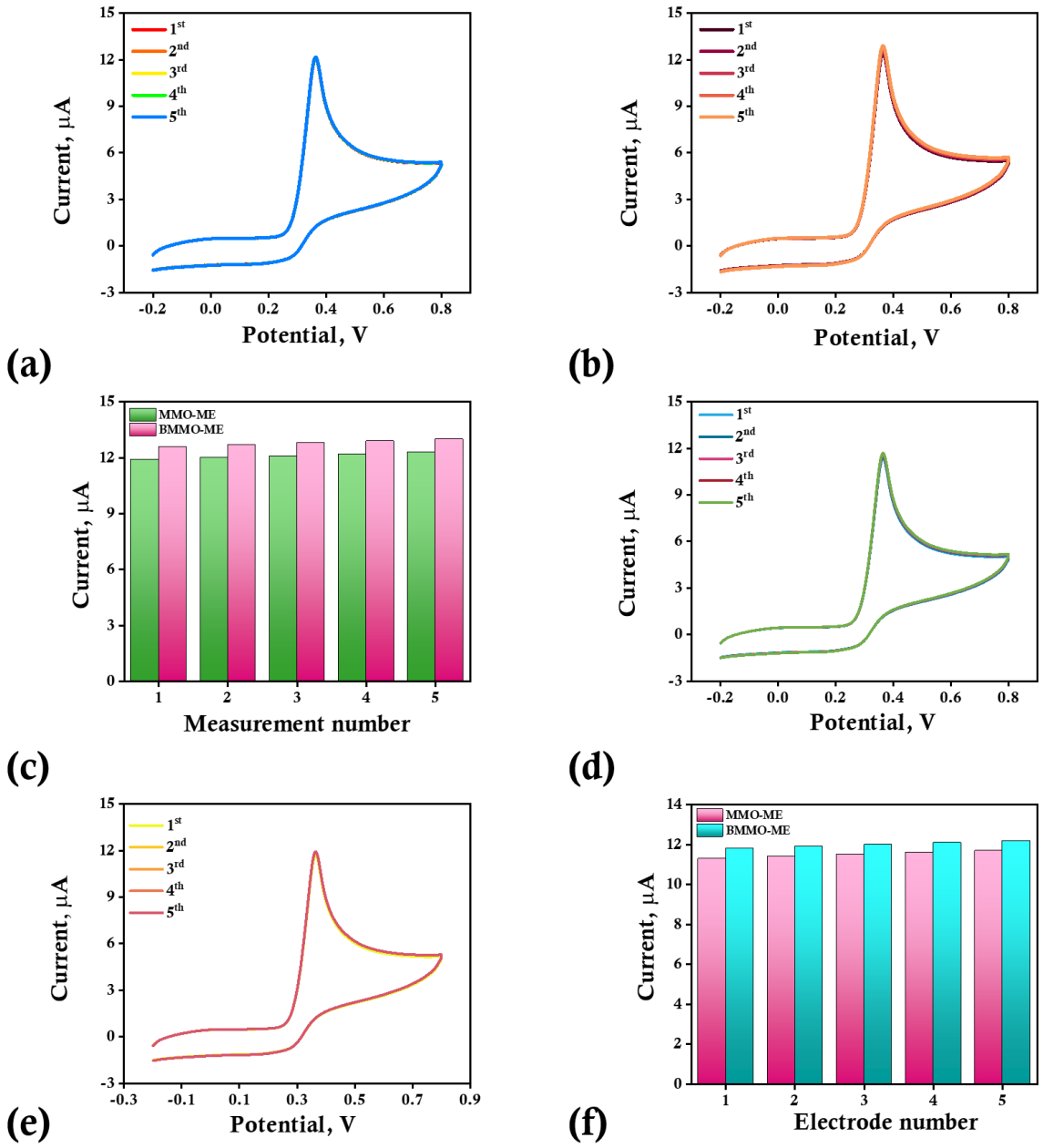


***Figure 7.*** *Repeatability CV responses of 1.0 mM UA in 0.2 M PBS (pH 7.0) at (a) MMO-ME and (b) BMMO-ME using the same electrode, (c) bar graph comparing the anodic peak currents obtained from five successive measurements using the same electrode, reproducibility CV responses obtained from five independently fabricated (d) MMO-ME and (e) BMMO-ME, (f) bar graph comparing the anodic peak currents obtained from five independently fabricated electrodes*

Figure 7b shows the responses of the CV under the identical repeatability test of the BMMO-ME. As in MMO-ME, peak currents do not vary, and the peak potential does not vary among repeated cycles. Notably, the maximum currents of BMMO-ME are always larger than those of MMO-ME, which can be explained by the change in the metallic component. Because of the two synergistically active metal oxides, catalytic site density increases and electron-transfer kinetics improve, enabling greater catalytic oxidation of UA [44]. This is corroborated by the DPV signals, which show that BMMO-ME is a reliable electrode for sensitive UA detection in repeated measurements.

Figure 7c provides a bar chart of the repeated data of MMO-ME and BMMO-ME. The graph indicates that the two electrodes exhibit similar peak currents across repeated scans, with BMMO-ME showing slightly higher and more stable currents. This comparison clearly shows a more catalytically

active and reproducible bimetallic-modified electrode. The uniformity of the data underscores the validity of the electrode design, demonstrating that both MMO-ME and BMMO-ME are viable platforms for routine UA monitoring. Figure 7d indicates that MMO-ME can be reproduced by testing independently fabricated electrodes under the same experimental conditions. The anodic peak currents are generally similar between electrodes, and the peak potentials vary little; therefore, the fabrication process yields electrodes with very uniform performance. Even small variations in current can be caused by small changes in paste composition, electrode-surface shape, or NP dispersion, which do not significantly affect the electrochemical response. These findings verify that MMO-ME has good reproducibility, which is needed in applications that require multiple electrodes, *e.g.* large biosensing or clinical diagnostics. The consistency of BMMO-ME across different electrode batches is shown in Figure 7e. The findings indicate that peak currents are constant and high across independently prepared electrodes, with little difference in anodic peak potentials [45]. The added reproducibility and stability of BMMO-ME over MMO-ME can be explained by a bimetallic synergistic effect, which, in turn, provides more homogeneously distributed active sites, reduced electron-transfer resistance, and stabilization of the electrode surface against fouling. This shows that BMMO-ME not only improves electrode sensitivity but also delivers strong performance.

A bar graph of the reproducibility findings for MMO-ME and BMMO-ME is presented in a consolidated form in Figure 7f. This is evident in the graph, as the peak currents differed very little across the different batches of electrodes, which validates the high level of reproducibility in both electrodes. BMMO-ME consistently yields better current responses than MMO-ME, indicating that it is a much better electrocatalyst and provides a more stable electrochemical interface. This value demonstrates that BMMO-ME is not only the most sensitive but also the most reliable and reproducible, making it the most suitable in practice when such UA sensing is in high demand, as consistent performance is essential. The repeatability of the MMO-ME and BMMO-ME electrodes was evaluated using successive measurements with the same electrode, yielding low RSD of 1.23 and 1.31 %, indicating excellent signal consistency. Reproducibility was assessed using independently prepared MMO-ME and BMMO-ME electrodes, showing RSDs of 1.33 and 1.41 %, respectively, confirming reliable electrode fabrication. Overall, the low RSD (<2 %) demonstrates the robustness and practical applicability of both MMO-ME and BMMO-ME sensing platforms.

Figures 8a to 8c present the Nyquist plots of the BE, MMO-ME, and BMMO-ME recorded in 1.0 mM UA in 0.2 M PBS (pH 7.0). The semicircle diameter in the high- to intermediate-frequency region corresponds to the interfacial charge-transfer resistance ($R_{ct}$). The apparent $R_{ct}$ values estimated from the semicircle diameters are approximately 52 Ω, 64 Ω and 63 Ω for BE, MMO-ME, and BMMO-ME, respectively. The modified electrodes exhibit comparable interfacial impedance responses, with BMMO-ME showing a slightly smaller apparent $R_{ct}$ than MMO-ME. The similar $R_{ct}$ values of MMO-ME and BMMO-ME indicate comparable interfacial charge-transfer characteristics under the investigated conditions.

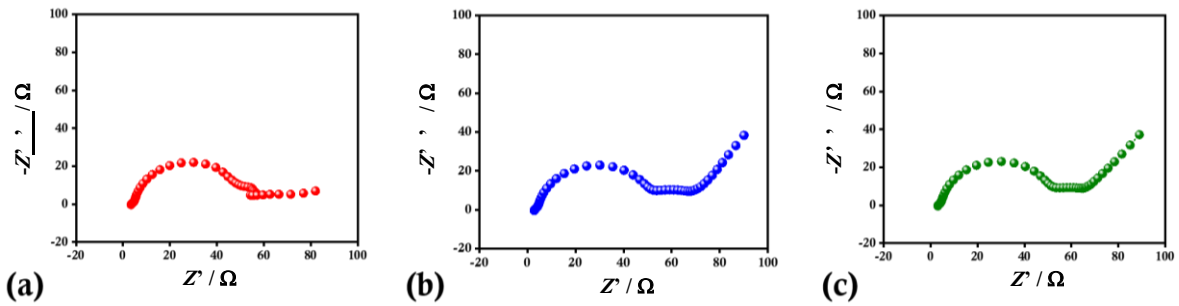


***Figure 8.*** *Nyquist plots of (a) BE, (b) MMO-ME, and (c) BMMO-ME recorded in 1 mM UA in 0.2 M PBS (pH 7.0)*

Figure 9 illustrates the DPV responses of the BE, MMO-ME, and BMMO-ME toward the simultaneous detection of dopamine (DA) and UA. Two distinct anodic oxidation peaks appear at approximately 0.15 and 0.26 V, corresponding to the oxidation of DA and UA, respectively, demonstrating sufficient peak separation for simultaneous detection. Compared with the BE, the MMO-ME and BMMO-ME electrodes exhibit enhanced anodic peak currents, with the UA oxidation peak becoming more prominent after electrode modification. Among the investigated electrodes, the BMMO-ME displays the highest UA oxidation current and the most well-defined oxidation peak, indicating superior electrocatalytic activity toward UA oxidation. This enhanced performance is attributed to the increased electroactive surface area, reduced charge-transfer resistance, and improved electron-transfer kinetics resulting from Bi incorporation into the MMO lattice. Furthermore, the clear separation of the DA and UA oxidation peaks indicates negligible mutual interference between the two electroactive species, confirming that the BMMO-ME enables the selective electrochemical determination of UA even in the presence of DA.

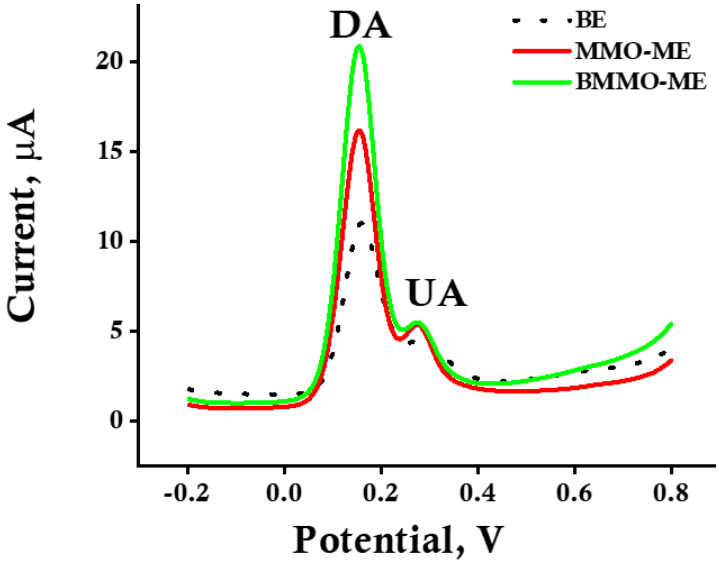


***Figure 9.*** *Simultaneous electrochemical detection of 1.0 mM DA and 1.0 mM UA in 0.2 M PBS, (pH 7.0) at the BE, MMO-ME and BMMO-ME*

*Real sample analysis of uric acid using tap water*

The practical applicability of MMO-ME for UA detection was evaluated through real-sample analysis using tap water. The collected tap water sample was filtered to remove suspended particulates, then spiked with known concentrations of UA (Table 1). Electrochemical measurements were then performed under optimized conditions. The MMO-ME exhibited well-defined anodic oxidation peaks for UA in the spiked tap water samples, indicating effective electrocatalytic activity even in a complex aqueous matrix. The measured UA concentrations closely matched the added values, yielding satisfactory recovery percentages with low relative standard deviation (RSD). These results confirm the good accuracy and reproducibility of the MMO-ME sensor [46]. The satisfactory recoveries indicate that the tap-water matrix did not substantially compromise the measured UA response under the tested conditions. The diffusion-controlled electron-transfer process and a stable electrode-electrolyte interface contribute to reliable sensing performance, demonstrating the feasibility of MMO-ME for real-sample analysis. The real sample applicability of the bimetallic MMO-modified electrode (BMMO-ME) was further assessed using tap water samples spiked with known concentrations of UA. After simple filtration pretreatment, electrochemical detection was carried out under the same optimized conditions. The BMMO-ME showed significantly

higher $I_{pa}$ and clearer signals than MMO-ME, resulting in improved recovery and lower RSD values. The excellent agreement between the detected and spiked UA concentrations confirms the high accuracy and precision of the BMMO-ME sensor [47]. This enhanced performance is attributed to the synergistic bimetallic effect, which increases the density of electroactive sites and accelerates electron-transfer kinetics. The negligible interference observed from tap water constituents highlights the strong selectivity of BMMO-ME toward UA oxidation. These results clearly demonstrate the robustness and reliability of the bimetallic electrode for real-world sample analysis, emphasizing its potential for practical environmental and clinical UA monitoring.

***Table 1.*** *Recovery of UA in tap water samples using MMO-ME and BMMO-ME*

| Sample | Amount added, µM | MMO-ME | | BMMO-ME | |
|---|---|---|---|---|---|
| | | Amount found, µM | Recovery, % | Amount found, µM | Recovery, % |
| 1 | 10 | 10.3 | 103 | 10.1 | 101 |
| 2 | 20 | 19.8 | 99 | 19.8 | 99 |
| 3 | 30 | 29.4 | 98 | 29.4 | 98 |

*Electrochemical sensing mechanism*

To better understand the enhanced electrochemical performance of the BMMO-ME electrode toward UA detection, a plausible electrochemical sensing mechanism is proposed based on the experimental results and the established oxidation pathway of UA. The mechanism involves sequential diffusion of UA from the electrolyte to the electrode surface, adsorption onto the electroactive Bi/Mn active sites, proton-coupled electron transfer, and subsequent hydrolysis of the oxidation intermediate to form the final product, allantoin. The proposed mechanism is illustrated in Figure 10.

The overall detection mechanism of UA at BMMO-ME involves three steps that can be described as follows:

Step 1: Diffusion of uric acid

UA molecules diffuse from the bulk PBS solution toward the BMMO-ME electrode surface. This diffusion process is represented by Equation (3):

$$UA_{(solution)} \rightarrow UA_{(surface)} \quad (3)$$

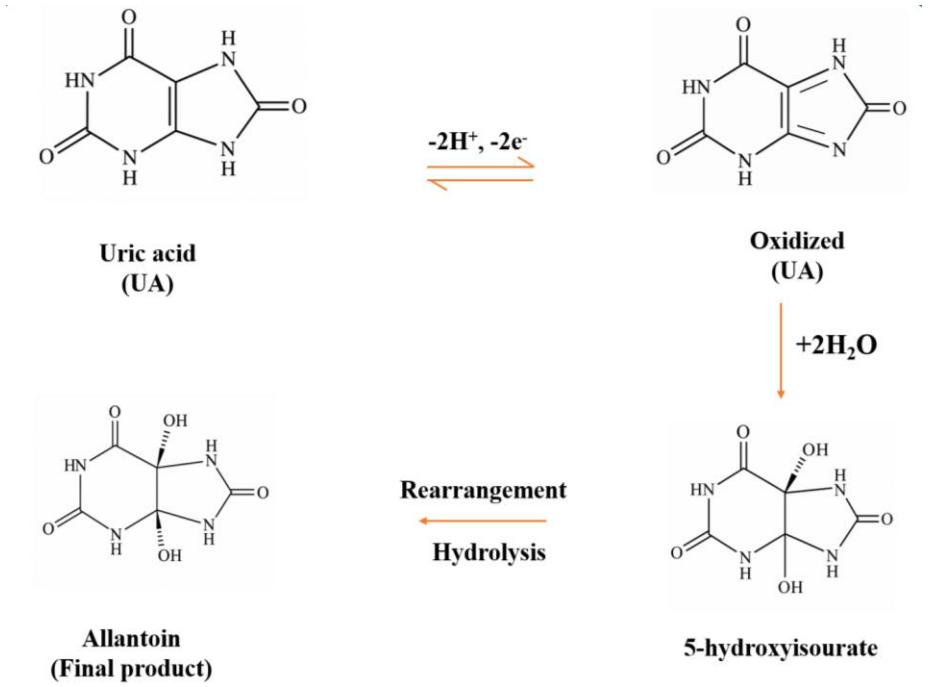


***Figure 10.*** *Proposed electrochemical oxidation mechanism of UA at the BMMO-ME*

http://doi.org/10.5599/jese.3475

Step 2: Adsorption

The diffused UA molecules are proposed to adsorb onto the electroactive Mn/Bi sites of the BMMO nanostructure before undergoing electrochemical oxidation. The proposed adsorption process is represented by Equation (4):

$$UA_{(surface)} + BMMO \rightarrow UA_{ads} \quad (4)$$

Step 3: Electron transfer

The adsorbed UA subsequently undergoes electrochemical oxidation, releasing two protons and two electrons. The proposed electron-transfer reaction is given in Equation (5):

$$UA_{ads} \rightarrow \text{Oxidized UA} + 2H^+ + 2e^- \quad (5)$$

UA molecules first diffuse from the bulk PBS to the BMMO-ME surface, where they are adsorbed onto the electroactive Bi/Mn active sites. The proposed mechanism is consistent with the commonly reported two-electron/two-proton oxidation pathway of UA, which forms the highly unstable intermediate 4,5-diiminohydantoin (DIH). DIH rapidly undergoes hydrolysis to produce 5-hydroxyisourate (5-HIU), which subsequently undergoes rearrangement and hydrolysis to form allantoin, the final oxidation product. During oxidation, the released electrons are efficiently transported through the conductive Bi-doped $MnMoO_4$ network to the graphite substrate, generating the anodic current. The enhanced electrochemical response of the BMMO-ME electrode is attributed to its larger electroactive surface area, abundant electroactive Bi/Mn active sites, and lower charge-transfer resistance, which collectively facilitate UA adsorption and accelerate interfacial electron-transfer kinetics.

## Conclusions

In this work, MMO based electrodes were developed and systematically evaluated for the electrochemical detection of UA. MMO-ME and BMMO-ME electrodes exhibited significantly improved electrocatalytic activity compared to the BE, with the Bi-doped system showing a clear performance advantage. Optimization of nanoparticle loading revealed that 4 mg provided the best balance between conductivity, electroactive surface area, and reproducibility. Under optimized conditions, UA oxidation followed a diffusion-controlled, proton-coupled mechanism and exhibited maximum response at physiological pH (7.0). DPV demonstrated a wide linear detection range of 10 to 60 nM, with low detection limits of 5.0 nM for MMO-ME and 4.5 nM for BMMO-ME. The enhanced sensitivity of BMMO-ME is attributed to the synergistic bimetallic effect, which increases active-site density, reduces overpotential, and improves interfacial charge-transfer kinetics. Both electrodes showed excellent stability, repeatability, and reproducibility, with relative standard deviation values below 2 %, while the BMMO-ME electrode exhibited superior resistance to surface fouling during repeated measurements. Reliable UA recovery values between 98 and 103 % in tap water samples further confirmed the practical applicability of the sensing platform. Overall, this study demonstrates that Bi-induced defect engineering is an effective strategy for activating manganese molybdate and establishes BMMO-ME as a robust, sensitive, and reliable electrochemical platform for real-time UA monitoring, with promising potential for clinical and physiological applications.

***Acknowledgments:*** *Authors extend their appreciation to Vidya Vikas Research & Development Centre for the facilities and encouragement. Princess Nourah bint Abdulrahman University Researchers Supporting Project number (PNURSP2026R86), Princess Nourah bint Abdulrahman University, Riyadh, Saudi Arabia.*

***Author contributions:*** *Conceptualization and Project administration: CSCK. Performed the experiments and analysed the data: KSML, MNR, MSA, PS, YHP & SC. All authors have written, reviewed, and read the manuscript.*

***Conflicts of interest:*** *The authors declare no conflict of interest.*

***Funding:*** *Princess Nourah bint Abdulrahman University Researchers Supporting Project number (PNURSP2026R86), Princess Nourah bint Abdulrahman University, Riyadh, Saudi Arabia.*

***Data availability:*** *The datasets used and/or analysed during the current study available from the corresponding author on reasonable request.*

## References

[1] D. J. Sutcliffe, A. R. Dinasarapu, J. E. Visser, J. D. Hoed, F. Seifar, P. Joshi, I. Ceballos-Picot, T. Sardar, E. J. Hess, Y. V. Sun, Z. Wen, M. E. Zwick, H. A. Jinnah, Induced pluripotent stem cells from subjects with Lesch-Nyhan disease, *Scientific Reports* **11** (2021) 8523. https://doi.org/10.1038/s41598-021-87955-9

[2] B. Mittal, D. P. Nanjappa, G. Chakraborty, A. Chakraborty, A. Khanna-Gupta, A patient with Lesch-Nyhan Syndrome presenting with anesthetic challenges: Not an exception, but the rule, *Gene Reports* **24** (2021) 101289. https://doi.org/10.1016/j.genrep.2021.101289

[3] H. Dey, S. S. Ali, V. A. Sethi, Deciphering the role of cell signaling pathways in gout pathogenesis and the therapeutic potential of phytoconstituents in their modulation, *Inflammopharmacology* **33** (2025) 2307-2323. https://doi.org/10.1007/s10787-025-01741-x

[4] A. Carr, Family therapy and systemic interventions for child-focused problems: The evidence base, *Journal of Family Therapy* **47** (2024) e12476. https://doi.org/10.1111/1467-6427.12476

[5] S. Javed, M. Fersini, G. Bernardini, Unleashing the Power of Induced Pluripotent Stem Cells in in vitro Modelling of Lesch-Nyhan Disease, *Stem Cell Reviews and Reports* **21** (2024) 304-318. https://doi.org/10.1007/s12015-024-10821-4

[6] M. Chen, J. Zhang, G. Ji, H. Wang, B. Zhu, C. Chen, H. Zhou, Y. Wang, Z. Gao, Universal flexible wearable biosensors for noninvasive health monitoring, *ACS Applied Materials & Interfaces* **17** (2025) 20741-20755. https://doi.org/10.1021/acsami.4c22623

[7] R. Rahimnia, A. Mohammadi, A. Pakdel, M. Gholamnejad, E. Zemanati, M. Khoshchehreh, *Molecular biology, genetic, and epigenetic urolithiasis*, in: Seyed Mohammad Kazem Aghamir (Ed.), *Genetics and Epigenetics of Genitourinary Diseases*, Academic Press, 2025, pp. 139-149, https://doi.org/10.1016/B978-0-443-27302-5.00009-7

[8] S. Zhou, X. Wen, D. J. Lessing, W. Chu, Uric Acid-Degrading *Lacticaseibacillus paracasei* CPU202306 Ameliorates Hyperuricemia by Regulating Uric Acid Metabolism and Intestinal Microecology in Mice, *Probiotics and Antimicrobial Proteins* **18** (2025) 411-435. https://doi.org/10.1007/s12602-025-10532-3

[9] L. Xu, C. Li, T. Wan, X. Sun, X. Lin, D. Yan, J. Li, P. Wei, Targeting uric acid: a promising intervention against oxidative stress and neuroinflammation in neurodegenerative diseases, *Cell Communication and Signaling* **23** (2025) 4. https://doi.org/10.1186/s12964-024-01965-4

[10] K. Mpofu, S. Chauke, L. Thwala, P. Mthunzi-Kufa, Aptamers and antibodies in optical biosensing, *Discover Chemistry* **2** (2025) 23. https://doi.org/10.1007/s44371-025-00094-2

[11] J. Narang, N. Rana, A. Chauhan, A. Kumari, V. Minhas, Accelerating the understanding of biosensors through the lens of cells: state of the field, emerging directions, advances, and challenges, *Applied Biochemistry and Biotechnology* **197** (2025) 4224-4262. https://doi.org/10.1007/s12010-025-05209-0

[12] A. Anwar, S. Rana, P. Pathak, Artificial intelligence in the management of metabolic disorders: a comprehensive review, *Journal of Endocrinological Investigation* **48** (2025) 1525-1538. https://doi.org/10.1007/s40618-025-02548-x

[13] K. Parwez, M. Izhar, A. Ahmed, N. Alturki, S. Abdullah, Smart Implantable Devices for cardiac health: a Novel Self-Powered wireless ECG monitoring system using energy harvesting and Machine Learning-Driven anomaly detection, *Smart Health* **37** (2025) 100582. https://doi.org/10.1016/j.smhl.2025.100582

[14] H. Rana, P. Singh, A.K. Agrahari, S. Yadav, *Environmental aspect of soft material*, Wiley Online Library, 2025, 467-491. https://doi.org/10.1002/9781394214143.ch16

[15] N. Zaidi, M.A. Mir, S.K. Chang, N. Abdelli, S.M. Hasnain, M.A.A. Khan, K. Andrews, Pharmaceuticals and personal care products as emerging contaminants: environmental fate, detection, and mitigation strategies, *International Journal of Environmental Analytical Chemistry* **105** (2025) 8837-8865. https://doi.org/10.1080/03067319.2025.2484456

[16] Y. Yin, J. Dai, B. Wang, L. Yan, Z. Long, W. Zhang, X. Su, W. Ji, L. Huang, L. Li, Wearable noninvasive glucose biosensors: biological metabolism, chemical sensing, and biological applications, *Advanced Materials Technologies* **10** (2025) e01311. https://doi.org/10.1002/admt.202501311

[17] J. Ma, S. Yang, Z. Yang, Z. He, Z. Du, Functional nanomaterials for advanced bioelectrode interfaces: recent advances in disease detection and metabolic monitoring, *Sensors* **25** (2025) 4412. https://doi.org/10.3390/s25144412

[18] S. Jabeen, P. Kumar, K. S. Samra, Optimizing electrochemical performance: Investigating the influence of oxidation of graphene oxide in rGO@$MnMoO_4$, *Journal of Alloys and Compounds* **981** (2024) 173673. https://doi.org/10.1016/j.jallcom.2024.173673

[19] M. Selvamani, A. Kesavan, A. Arulraj, P.C. Ramamurthy, M. Rahaman, S. Pandiaraj, M. Thiruvengadam, E. J. S. Sacari, E. M. L. Sandoval, M. R. Viswanathan, Microwave-Assisted synthesis of flower-like $MnMoO_4$ nanostructures and their photocatalytic performance, *Materials* **17** (2024) 1451. https://doi.org/10.3390/ma17071451

[20] J.V . Kumar, R. A. Elkaffas, S. Eissa, Unleashing the power of MnMoO4/rGO nanocomposite towards the electrochemical aptasensing of neurotoxic pesticide fenitrothion, *Electrochimica Acta* **536** (2025) 146708. https://doi.org/10.1016/j.electacta.2025.146708

[21] L. Feng, S. Song, H. Li, R. He, S. Chen, J. Wang, G. Zhao, X. Zhao, Nano-Biosensors based on noble metal and semiconductor materials: Emerging trends and future Prospects, *Metals* **13** (2023) 792. https://doi.org/10.3390/met13040792

[22] F. Pan, B. Peerless, S. Dehnen, Bismuth-Based Metal Clusters-from molecular aesthetics to contemporary Materials Science, *Accounts of Chemical Research* **56** (2023) 1018-1030. https://doi.org/10.1021/acs.accounts.3c00020

[23] O. Sreelakshmi, S. F. Sameera, M. A. Shafna, V. L. N. M. A. Mini, N. M. Muzzammil, N. Nasirin, S. M. A. Shibli, Tuning of oxygen vacancies to control color and electron dynamics in alkali metal substituted bismuth layered oxides for energy-efficient coatings, *Journal of Materials Chemistry C* **13** (2025) 8641-8649. https://doi.org/10.1039/d4tc05512h

[24] X. Chen, Y. Wu, Y. Qin, R. Carmieli, I. Popov, V. Gutkin, C. Fan, I. Willner, Molecularly imprinted Polyaniline-Coated Cu-Zeolitic imidazolate framework nanoparticles: Uricase-Mimicking "Polynanozyme" catalyzing uric acid oxidation, *ACS Nano* **19** (2025) 9981-9993. https://doi.org/10.1021/acsnano.4c16272

[25] A. Pane, S. Vicenzi, C. Mattioli, D. Mordini, A. Menichetti, M. Montalti, Melanin-Related materials in electrochemical sensors for monitoring the environment and food, *Biosensors* **15** (2025) 631. https://doi.org/10.3390/bios15090631

[26] F. Ahmad, S. Zahid, M. I. Khan, A. Shanableh, N. Farooq, K. A. Rao, M. B. Taj, S. Manzoor, L. G. Voskressensky, R. Luque, Direct electron transfer chemistry of redox-active enzymes: applications in biosensor development, *Biofuels, Bioproducts and Biorefining* **19** (2025) 963-981. https://doi.org/10.1002/bbb.2742

[27] J. Wang, Z. Qing, X. Zhou, H. Zou, H. Li, A. Liu, S. Duan, Y. Li, Crystal structure, Raman spectra, bond characteristics, and microwave dielectric properties of $MnMoO_4$ ceramics, *Ceramics International* **49** (2023) 23627-23633. https://doi.org/10.1016/j.ceramint.2023.04.197

[28] S. Cheng, H. Yu, M. Zhang, R. Liu, Y. Zhang, Z. Xu, T. Guo, M. Xie, Y. Yang, R. Yu, Synthesis and applications of $Eu^{3+}$, $Na^{+}$-doped high-color-purity $BaSrGa_4O_8$ red phosphors for w-LEDs and the detection of latent fingerprints, *Journal of Photochemistry and Photobiology A: Chemistry* **470** (2026) 116613. https://doi.org/10.1016/j.jphotochem.2025.116613

[29] P. Debye, P. Scherrer, Interferenzen an regellos orientierten 21eilcheni m Röntgenlicht. I., Nachrichten von der Gesellschaft der Wissenschaften zu Göttingen, Mathematisch-Physikalische Klasse **1916** (1916) 1-15. http://eudml.org/doc/58947 (In German)

[30] X. Zeng, Y. Zhang, X. Li, C. Wang, X. Xia, C. Jin, D. Huo, C. Hou, Nickel-Platinum Double-Atom catalysts for Real-Time dopamine detection in sweat and potential applications in flexible Zinc-Air batteries, *Analytical Chemistry* **97** (2025) 12090-12099. https://doi.org/10.1021/acs.analchem.5c00239

[31] T. Zhang, D. Ma, F. Cai, A novel and sensitive AuNPs/tetracystein-glucose dehydrogenase (GDH)/screen-printed electrode(SPE)-based electrochemical glucose biosensor, *Microchemical Journal* **216** (2025) 114629. https://doi.org/10.1016/j.microc.2025.114629

[32] M. Wang, H. Zheng, L. Yang, L. Jiang, Multi parameter sweat detection system based on screen printed electrodes, *Sensing Imaging* **26** (2025) 136. https://doi.org/10.1007/s11220-025-00662-x

[33] C. Ji, X. Tang, L. Wang, Y. Han, J. Wei, L. Wu, High-Performance ratiometric magnetic electrochemical sensor for acetamiprid detection using AG@PDA@$Fe_3O_4$ nanocomposites, *Journal of Food Composition and Analysis* **137** (2024) 106914. https://doi.org/10.1016/j.jfca.2024.106914

[34] S. S. Soliman, A. M. Mahmoud, A. A. Mouhamed, O. G. Hussein, Electrochemical sensor modified with heterostructure of graphitic carbon nitride/gold nanoparticles for non-invasive uric acid detection in saliva, *Sensing and Bio-Sensing Research* **50** (2025) 100881. https://doi.org/10.1016/j.sbsr.2025.100881

[35] A. Joshi, G. Slaughter, NiFeCo-modified bucky paper electrodes for sensitive and selective uric acid detection, *Microchemical Journal* **208** (2024) 112348. https://doi.org/10.1016/j.microc.2024.112348

[36] Sehrish, R. Manzoor, J. Li, H. Yang, R. Cai, Dual enzyme mimetic activities of CUBIZR@PAH nanocomposites for enzyme free colorimetric detection of glucose and uric acid, *Advanced Materials Technologies* **19** (2025) e00693. https://doi.org/10.1002/admt.202500693

[37] Z. Wang, Y. Chen, Z. Chen, J. Duan, H. Wang, E. Guo, J. Zhi, S. Shuang, C. Dong, J. Li, X. Gong, A Trinity Sensing platform for uric acid detection in clinical samples using FE-Functionalized Carbon Quantum Dot nanozymes, *Talanta* **293** (2025) 128007. https://doi.org/10.1016/j.talanta.2025.128007

[38] F. Mazzara, B. Patella, G. Aiello, A. O'Riordan, C. Torino, A. Vilasi, R. Inguanta, Electrochemical detection of uric acid and ascorbic acid using r-GO/NPs based sensors, *Electrochimica Acta* **388** (2021) 138652. https://doi.org/10.1016/j.electacta.2021.138652

[39] H. R. Li, H. Xu, Z. Y. Zheng, G. H. Li, Z. Y. You, S. S. Li, Strategic defect engineering and valence modulation in B-doped $CeO_2$ nanoparticles for highly sensitive and reliable electrochemical detection of p-nitrophenol, *Microchimica Acta* **192** (2025) 608. https://doi.org/10.1007/s00604-025-07486-2

[40] V. B. Jaryal, A. Villa, N. Gupta, Metal-Free Carbon-Based Nanomaterials: Insights from Synthesis to Applications in Sustainable Catalysis, *ACS Sustainable Chemistry & Engineering* **11** (2023) 14841-14865. https://doi.org/10.1021/acssuschemeng.3c01452

[41] J. Sun, G. Wang, H. Zhang, B. Zhang, C. Hu, Facile fabrication of a conductive polypyrrole membrane for anti-fouling enhancement by electrical repulsion and in situ oxidation, *Chemosphere* **270** (2020) 129416. https://doi.org/10.1016/j.chemosphere.2020.129416
[42] L. Dong, X. Wu, D. Zhang, J. Zhu, L. Liu, C. Liu, X. Zhang, Z. Tong, Fabrication of polyfluorinated azobenzene-functionalized carbon nanotubes for detecting dopamine and uric acid, *Journal of Applied Electrochemistry* **56** (2025) 18. https://doi.org/10.1007/s10800-025-02419-6
[43] M. G. Bruno, M. Gutiérrez-Capitán, B. Patella, G. Aiello, R. Inguanta, C. Fernández-Sánchez, Paper-based microfluidic electrochemical sensor for chloride ion and uric acid detection in sweat, *Talanta* **298** (2025) 128969. https://doi.org/10.1016/j.talanta.2025.128969
[44] H. Inoue, S. Takashi, Relationship between changes in uric acid levels and renal function during 12 months of treatment with luseogliflozin, *Diabetology International* **17** (2025) 7. https://doi.org/10.1007/s13340-025-00853-7
[45] S. Saidi, M. Mirzaei, M. Torkzadeh-Mahani, M. Barani, Multivariate analysis and electrochemical detection of uric acid using a novel Fe-Ni-MOF/RGO nanosheet-based uricase biosensor on glassy carbon electrode, *Journal of Experimental Nanoscience* **21** (2025) 2598531. https://doi.org/10.1080/17458080.2025.2598531
[46] Z. Wang, J. Liu, T. Liu, L. Yi, Z. Xiao, Z. Deng, S. Gong, Anti-Interference Bimodule Biosensors with Au/$Cu_2O$ Hollow Spheres for Accurate Detection of Uric Acid in Human Serum, *Nanoscale* **18** (2026) 3095-3104. https://doi.org/10.1039/d5nr04790k
[47] M. Kuwabara, R. Ae, K. Kosami, M. Kanbay, A. Andres-Hernando, I. Hisatome, M.A. Lanaspa, Current updates and future perspectives in uric acid research, *Hypertension Research* **48** (2024) 867-873. https://doi.org/10.1038/s41440-024-02031-9